Three-dimensional and non-destructive characterization of nerves inside conduits using laboratory-based micro computed tomography

Christos Bikis [a], Peter Thalmann [a], Lucas Degrugillier [b], Georg Schulz [a], Bert Müller [a,*], Daniel F. Kalbermatten [c,d], Srinivas Madduri [b,c,e,**], Simone E. Hieber [a,***]

[a] Biomaterials Science Center, Department of Biomedical Engineering, University of Basel, Switzerland
[b] Center for Bioengineering and Regenerative Medicine, Department of Biomedical Engineering, University of Basel, Switzerland
[c] Department of Plastic, Reconstructive, Aesthetic and Hand Surgery, Basel University Hospital, Switzerland
[d] Department of Pathology, University Hospital, Switzerland
[e] Department of Biomedicine, University of Basel, Switzerland

HIGHLIGHTS

- 3D imaging of paraffin-embedded peripheral nerves without contrast agent achieved.
- Micro-anatomical features of nerves resolved even inside conduit.
- Automatic nerve segmentation despite of characteristic artifacts.
- Automatic extraction of anatomical parameters in a few minutes for a 100 mm³ volume.

GRAPHICAL ABSTRACT
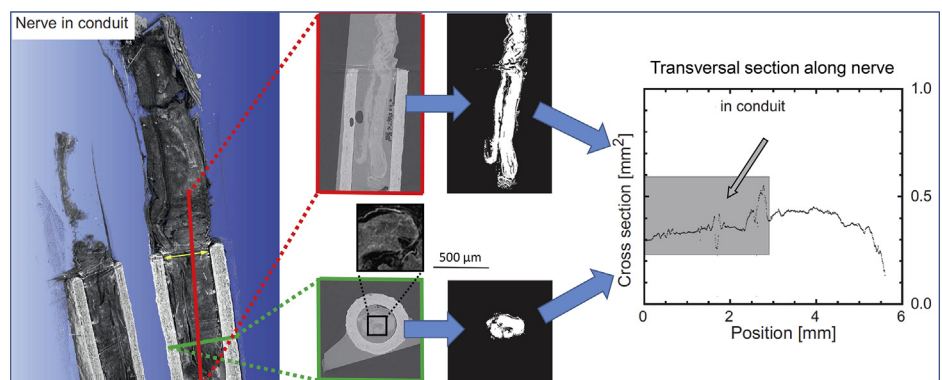
ARTICLE INFO

ABSTRACT

Background: Histological assessment of peripheral nerve regeneration in animals is tedious, time-consuming and challenging for three-dimensional analysis.
New method: The present study reports on how and to what extent micro computed tomography of paraffin-embedded samples can provide a reliable three-dimensional approach for quantitative analysis of peripheral nerves.
Results: Rat sciatic nerves were harvested, formalin-fixated, positioned into nerve conduits (NC), paraffin-embedded, and imaged using a laboratory-based X-ray microtomography system with an isotropic voxel length of 4 μm. Suitable quantitative measures were identified and automatically evaluated, i.e. nerve length, cross-sectional area and volume, as well as vascular structures, to be used as an assessment and comparison indicator of regeneration quality.

Comparison with existing methods: Compared to imaging using contrast agents, the investigated specimens can subsequently undergo the conventional histological analysis without requiring additional preparation steps. Contrast and spatial resolution are also increased significantly.

Conclusions: We demonstrate the potential of the micro computed tomography for non-destructive monitoring of peripheral nerves inside the conduits.

1. Introduction

Histology and histopathology focus on the study of cellular and tissue microanatomy in health and disease, respectively. They play a prominent role, both in research and clinical practice and are based on the main principle of examining tissue slices under an optical microscope. In several applications, however, this approach is not straightforward. In vivo imaging methods for monitoring axon growth using fluorescence lack micrometer resolution and offer a maximal penetration depth close to 2 mm (Kerschensteiner et al., 2005). Immunohistochemicial staining is the gold standard for the analysis of regenerated nerve tissue, but exhaustive serial sectioning is demanding for the evaluation in three dimensions (Godinho et al., 2013; Madduri et al., 2010b). Electron micrographs offer a high degree of lateral resolution, but the approach is associated with sample size constraints (Godinho et al., 2013).

It is known that X-ray microtomography (μCT) of soft tissues and nerves scanned in aqueous solutions provides images with limited contrast, due to the weak difference of tissue constituents in X-ray absorption. Therefore, iodine as contrast agent, has been applied for the X-ray imaging of nerves in conduits (Hopkins et al., 2015). Very recently it has been demonstrated that paraffin embedding of human cerebellum allows for the visualization of individual Purkinje cells without staining, using a laboratory μCT system (Khimchenko et al., 2016) and their segmentation using feature-based filtering of synchrotron radiation μCT data (Hieber et al., 2016). We hereby assume such a label-free approach is also suitable for peripheral nerves, that have a great demand for high-throughput regeneration monitoring. Hence, we propose to employ a multi-step procedure combining tissue preparation, laboratory micro computed tomography and tailored image analysis to quantitatively characterize regenerating nerves inside an absorbable nerve conduit (NC) in a true three-dimensional manner. This non-destructive method will be applied before the preparation of histological sections, also aiding in the selection of the appropriate cutting planes (Stalder et al., 2014). For this feasibility study, healthy rat sciatic nerves were explanted and embedded in paraffin inside and outside a collagen NC (Madduri et al., 2010a).

In order to exhaust the full capacity of micro computed tomography (Holme et al., 2014), excess paraffin was removed as required, by means of applying a specific preparation protocol. Tomography data were acquired with high contrast and analyzed by a software developed for both rat nerves with and without NC. Identical anatomical details were identified in both cases. Additionally, the volume, area and length of the investigated nerves and their vasculature were also calculated in an automated approach, allowing for high-throughput investigations of nerve regeneration.

2. Materials and methods

The study was conducted in compliance with the ethical instructions of the Veterinary Office of the Kanton of Basel-Stadt (Basel, Switzerland), permission number 25212. Three sciatic nerves were surgically extracted from healthy Sprague Dawley rats. Collagen NCs were fabricated by spinning mandrel technology, as illustrated previously (Madduri et al., 2010a). Insoluble collagen (2.5%, w/w) was swollen in 1 M acetic acid and homogenized with a high-speed mixer at 10,000 rpm (Polytron®, Kinematica, Lucerne, Switzerland) for 1 min. The homogeneous collagen dispersion was applied via a syringe onto a spinning Au-coated mandrel (diameter of 1.5 mm), installed in a sideways reciprocating apparatus, and the solvent was dried off under laminar airflow. The resulting tubes were neutralized by incubation in 0.1 M di-sodium hydrogen phosphate (pH of 7.4) for 1 h. The tubes were finally cut into 14 mm long specimens, which were cross-linked by physical means, i.e. by subjecting the collagen tubes to a dehydro-thermal treatment (DHT) at a temperature of 110 °C and a pressure of 20 mbar for 5 days. The resulting tubes exhibited an outer diameter of 2.5 mm and inner diameter of 1.5 mm.

The nerves were fixed in formalin solution and subsequently embedded in paraffin blocks according to standard histological preparation. In order to optimize the specimen's diameter for the tomography and to avoid entrapped air bubbles the paraffin embedding procedure was optimized. The long nerve was cut in two parts for ease of placing the nerve segments inside the conduit and further to avoid any tissue deformation over the course of tissue alignment along the lumen of the NC. After inserting the two segments of nerve, each from the opposite opening of NC, the NC-nerve complex was embedded in paraffin.

The μCT system used for this study was the nanotom® m (phoenix |X-ray, GE Sensing & Inspection Technologies GmbH, Wunstorf, Germany). It is equipped with a 180 kV nanofocus transmission source and a 3072 × 2400 pixels GE DXR detector. For all the presented measurements, the acceleration voltage was set to 60 kV and the beam current to 280 μA. Source-to-specimen and source-to-detector distances were 9 mm and 225 mm, respectively, resulting in an effective pixel size of 4 μm. For all specimens, 1800 projections were acquired equiangularly over the range of 360°. In order to increase photon statistics, nine images with an exposure time of 0.5 s each were averaged at each angular position. This resulted in a total scanning time of 150 min for one height step covering a nerve section 9.6 mm long. For specimens longer than 9.6 mm, two or more height steps were acquired and stitched after reconstruction (Müller et al., 2012).

To reduce the effect of faulty detector pixels appearing constantly dark or bright in the projections, the acquired radiographs were filtered with a 2D median filter with a 3 × 3 kernel using the open-source software ImageJ (Schneider et al., 2012), prior to reconstruction. Thereby the contrast considerably increased, as found in the related absorption histograms, at the expense of negligible blurring. The filtered radiographs were reconstructed using the nanotom® m manufacturer's software phoenix datosx 2.0.1 – RTM (GE Sensing & Inspection Technologies GmbH, Wunstorf, Germany), which employs a modified Feldkamp cone beam reconstruction algorithm. Subsequently, the three-dimensional datasets were imported in the VGStudio MAX 2.1 (Volume Graphics GmbH, Heidelberg, Germany) software and scaled to the same gray-scale range necessary for image analysis. These 16-bit datasets have a size of approximately 2 GB considering 1 cm of nerve. The VGStudio

MAX was used for the three-dimensional rendering of the acquired tomograms.

For the morphological analysis, the paraffin-embedded nervous tissue, partly within the conduit, has to be segmented. Related steps of this procedure are illustrated in Fig. 1. Image (a) represents the raw data. Image (b) shows that the contrast in the raw data was sufficient to successfully apply the Otsu method (Otsu, 1979), in order to digitally remove the scaffold. A distance transform served for removing a thin part (3–6 voxels) of the remaining specimen's surface, which was followed by selecting the largest connected component (c). This step was particularly needed to separate the specimen from heavy streaking and artifacts caused by the remaining air bubbles. As the artifacts were removed from the histograms, a second thresholding step using Otsu's method was applied (d). Given that the Gaussian distributions of the bare paraffin and the paraffin-embedded specimen in the absorption histograms were insufficiently separated, this second thresholding step did not result in perfect virtual paraffin removal and created some voids inside the tissue. Such kind of noise was removed using a 2D median filter with a kernel of size 3×3 (e). The segmentation was finalized by selecting the largest connected component and applying an adaptive void-filling filter (f). After segmentation, the nerve was skeletonized by calculating the geometrical center for each slice. The entire segmentation and analysis procedure was performed in Matlab (MATLAB 2016a, The MathWorks, Inc., Natick, Massachusetts, United States).

Since the X-ray absorption values of the vessels overlap with the ones of other structures, a feature-based segmentation is applied to segment them. The probability of a voxel to belong to a vessel is determined by the established Frangi-Filter that examines the eigenvalues of the Hessian matrix (Frangi et al., 1998). The filter parameters were chosen to $\alpha = 0.1$, $\beta = 0.1$, $\gamma = 0.2$ in the Matlab implementation by Kroon (2009). The voxel range was between one and three and the threshold of vesselness 0.4 for the normalized dataset.

3. Results

3.1. Descriptive evaluation

Fig. 2 compares representative slices of two CT datasets showing the same nerve. In the presented cross sections one can readily recognize the microanatomy of the selected nerve. In particular, the components including the epineurium and perineurium membranes surrounding the main axonal mass can be identified. The characteristic microanatomy of the nerve fascicle bundles is also visible. At some positions, the vasa nervorum (white-colored arrowheads) inside the nerve bulk exhibit a considerably higher X-ray absorption than their surrounding nervous tissue.

The left section also contains the porous conduit, which can be quantitatively characterized as well. Both the surface morphology as well as the locations and sizes of the individual pores inside the scaffold material are accessible.

In general, the nerve visualization inside the conduit is challenging because of its relatively high X-ray absorption. Artifacts such as streaks impede a detailed description. The images demonstrate, however, that the present experimental setup enables us to obtain results without significant differences between the bare nerve and the nerve within the conduit. The remaining differences are limited deformations, a result of nerve handling between the acquisitions of the tomograms. Streak artifacts are rare.

Contrary to histology, tomography not only allows two-dimensional imaging in predefined directions but also the three-dimensional rendering with isotropic voxel size. Fig. 3 shows

Table 1
Measured geometrical parameters of three selected nerves.

Sample number	Volume (mm^3)	Length (mm)	Average cross section (mm^2)
1	3.54 ± 0.39	9.59 ± 0.23	0.45 ± 0.05
2	1.81 ± 0.20	11.00 ± 0.28	0.34 ± 0.04
3	2.81 ± 0.31	11.92 ± 0.38	0.47 ± 0.05

an exemplary rendering, where a selected specimen is virtually cut into two parts along the symmetry axis. The internal structure of the two rat sciatic nerve segments, the gap between them, as well as the surrounding conduit can be simultaneously visualized.

3.2. Nerve segmentation

The quantification of nerve regeneration requires the identification of the nervous tissue within the three-dimensional dataset. The contrast, density resolution, of the CT data enables a clear distinction between the air, the paraffin, the scaffold, and the nervous tissue based on their specific X-ray attenuation. Thus, a thresholding approach (Müller et al., 2002) performs well for the segmentation as illustrated in Fig. 1, cp. especially images (b) and (d). Imaging artifacts at the surface and noise due to photon statistics can be handled appropriately by filtering techniques see images (c), (e) and (f). As a result, the segmentation mask in Fig. 1(f) matches well with the nervous tissue shown in the non-treated dataset (Fig. 1(a)). Even thin layers of nervous tissue including the epineurium and perineurium membranes are represented clearly.

3.3. Nerve characterization by geometrical parameters

The contrast in the tomography data was sufficient to automatically segment the nerve. The success of the procedure was manually validated. For this purpose, two experts compared the original and related segmented data section-wise.

In a subsequent step, the segmented nerve was charted to extract the morphological data, i.e. volume, length, and cross section. Table 1 lists these geometrical parameters for the three selected nerves.

Although μCT provides true micrometer resolution, the error bars are rather large. Inaccuracy is caused by discontinuities in the curve progression, as indicated in Fig. 4. These discontinuities are caused by streak artifacts, due to high X-ray absorbing species. Therefore, the streaks are more frequently found at conduits and their interfaces (Fig. 4).

From the anatomical point of view, the cross-sectional area should be consistent from section to section. Therefore, the smoothness of the curves in the diagrams of Fig. 4 is an indicator for the reasonable performance of the automatic segmentation.

3.4. Vessel visualization

Fig. 5 shows the segmented vessels after filtering the three-dimensional dataset for tubular structures. At some positions the segments are apparently connected to streak artifacts, which impedes their segmentation. In general, one recognizes the course of the vessels, although they are frequently interrupted within the acquired three-dimensional data. The related virtual sections prove the significantly higher X-ray absorption of the segmented parts of the visualized blood vessel system.

4. Discussion

The microanatomy of rat peripheral nerves has been studied in detail, see e.g. Bertelli et al. (1995). The quality of the present CT slices is almost comparable to the slides of digitized histology with
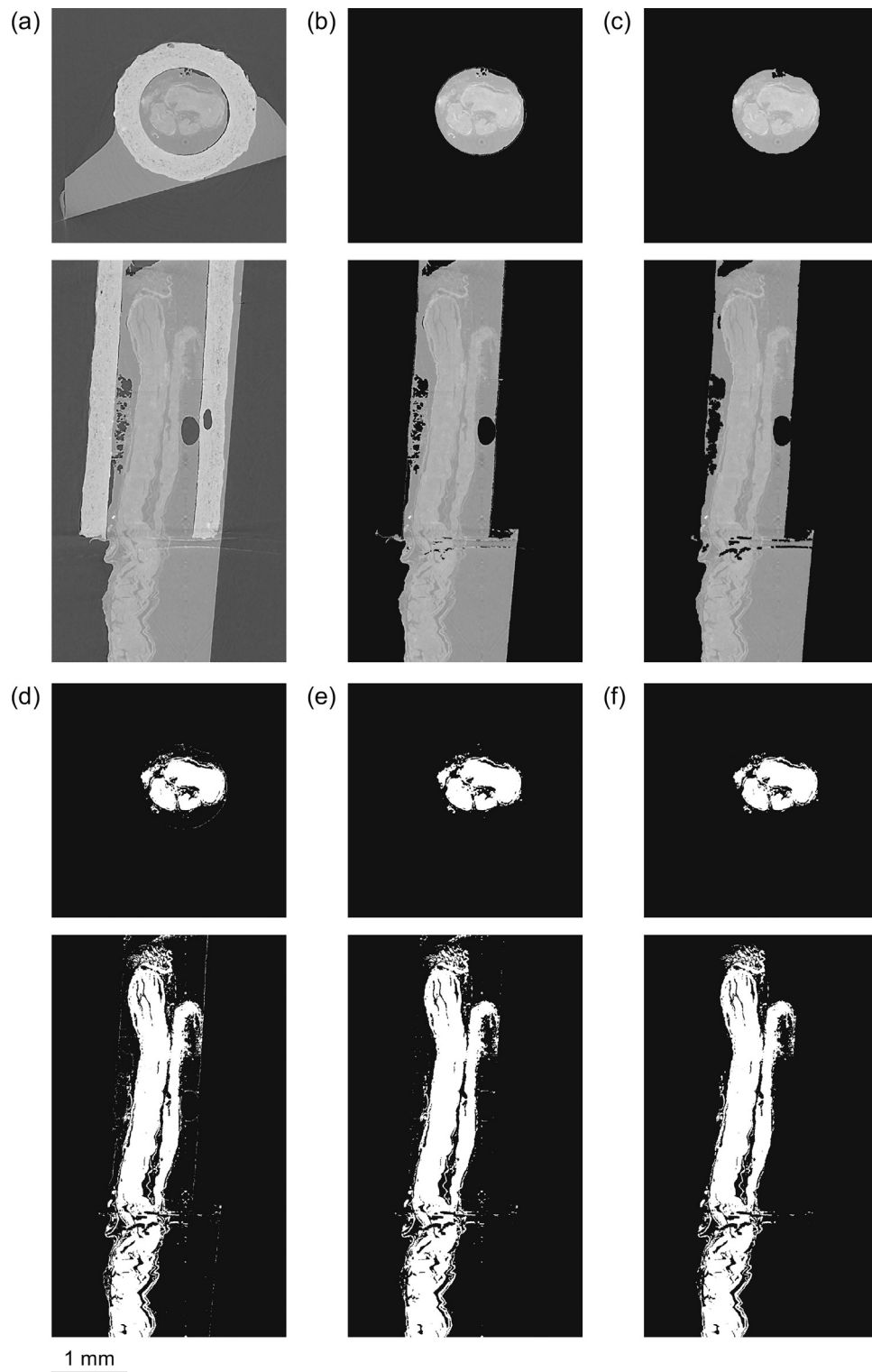
Fig. 1. A cross-sectional and a longitudinal section of a selected dataset before and after segmentation: (a) original, (b) air and scaffold virtually removed, (c) boundary eroded and largest object selected, (d) paraffin virtually removed and dataset binarized, (e) median filtered and (f) largest object selected and voids filled.

medial magnification. Previous imaging data were mainly obtained optically and restricted in two dimensions showing the nerve's surface or selected cross sections, or the third direction of the data set was hardly resolved better than 50 μm. The performance of imaging techniques including micro computed tomography can be characterized by the spatial and density resolution (Thurner et al., 2004). Whereas the accessible spatial resolution only depends on

the experimental setup and the components included, the density resolution (contrast) crucially depends on the specimen preparation, i.e. dehydration, embedding, and staining. CT-systems for animal experiments with a rotating gantry, as used by Hopkins et al. (2015) are usually not stable enough to reach a spatial resolution below 20 μm. Using advanced micro computed tomography systems based on nanofocus X-ray tubes, such as nanotom® m, one
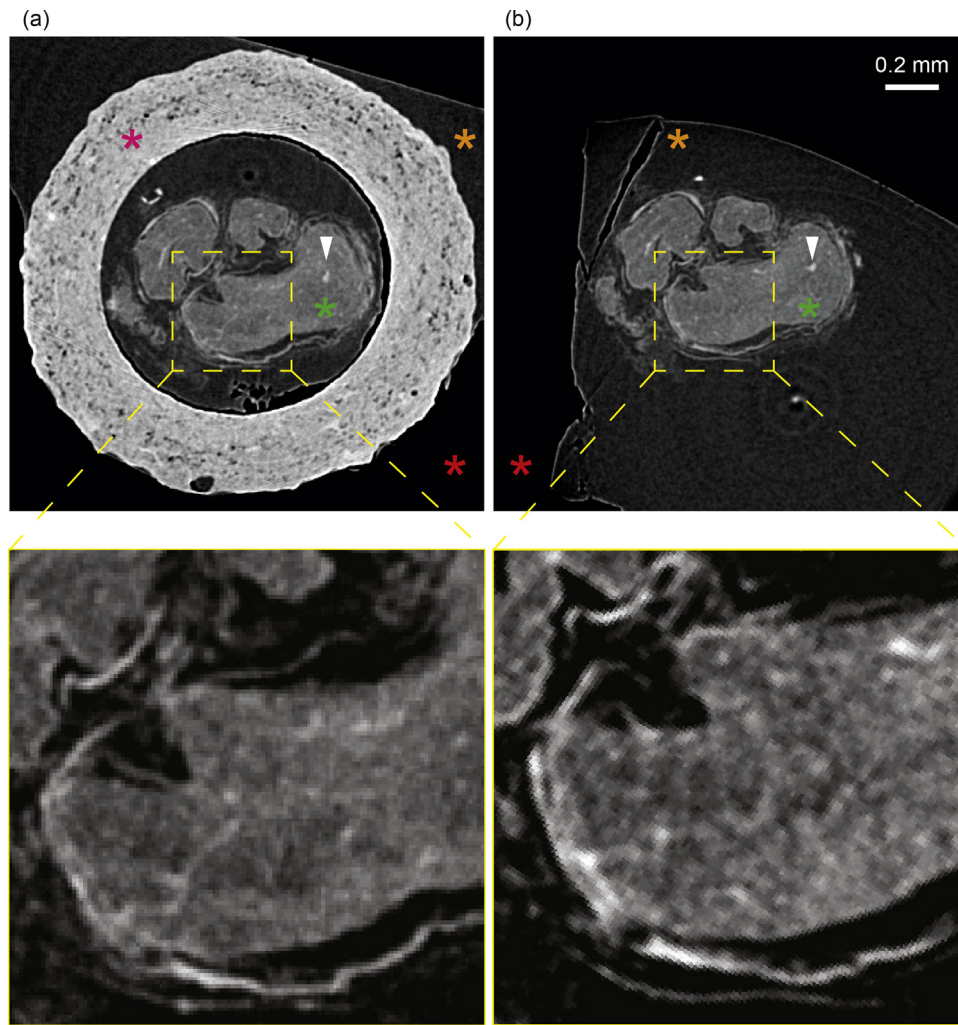
Fig. 2. (a) A cross-sectional view of a rat sciatic nerve (green-colored asterisk) inside the collagen scaffold (magenta-colored asterisk). The nerve-scaffold complex is embedded in paraffin (orange-colored asterisk). The lowest absorbing element in the picture is the air (red-colored asterisk). (b) Related section of the same nerve subsequently scanned without the conduit. Higher X-ray absorption values are represented by lighter gray shades.
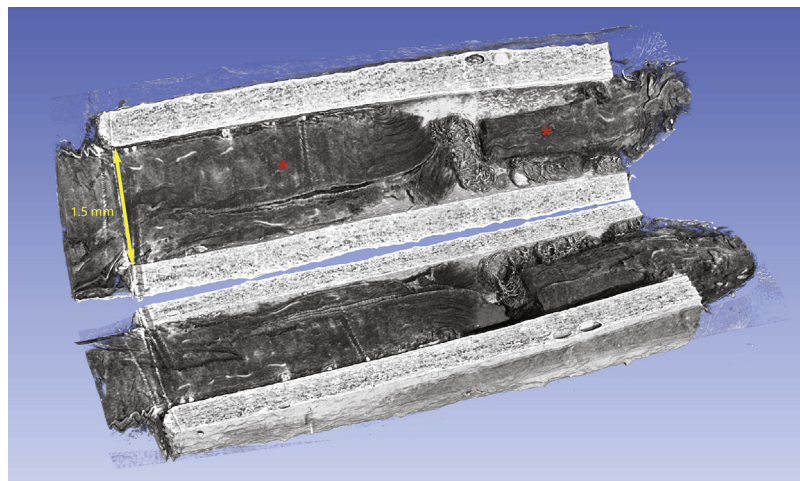

Fig. 3. A three-dimensional view of a selected nerve specimen comprised of two parts (red-colored asterisks) inside a collagen scaffold. The specimen was digitally sectioned, and the paraffin was made transparent. The two components visible are the rat sciatic nerve tissue (gray) and the collagen scaffold (white). The NC has a length of 14 mm and an inner diameter of 1.5 mm.

can achieve a spatial resolution below 1 μm. The effective spatial resolution, however, also depends on the maximal diameter of the specimen and the detector pixels (Holme et al., 2014). Therefore, the effective pixel size in the present study was restricted to 2 μm based on the specimens' dimensions. In order to improve acquisition time and image quality and to avoid sample deformation as a
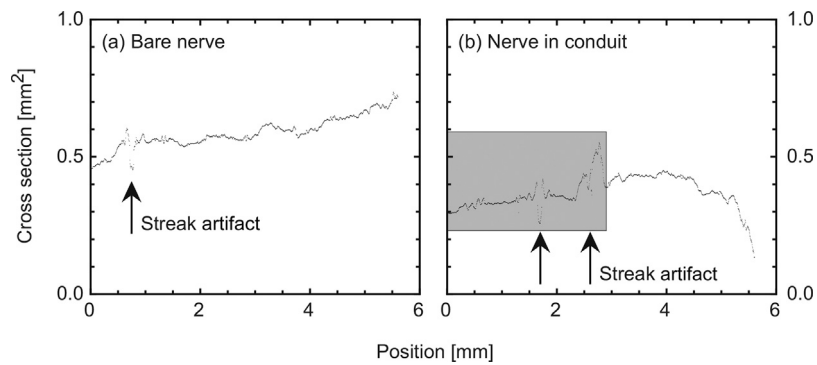
Fig. 4. The cross-sectional area along the longitudinal direction of the specimen; (a) bare nerve and (b) nerve inside the conduit. Discontinuities as indicated by the arrows relate to streak artifacts and are more frequently found at the NC.
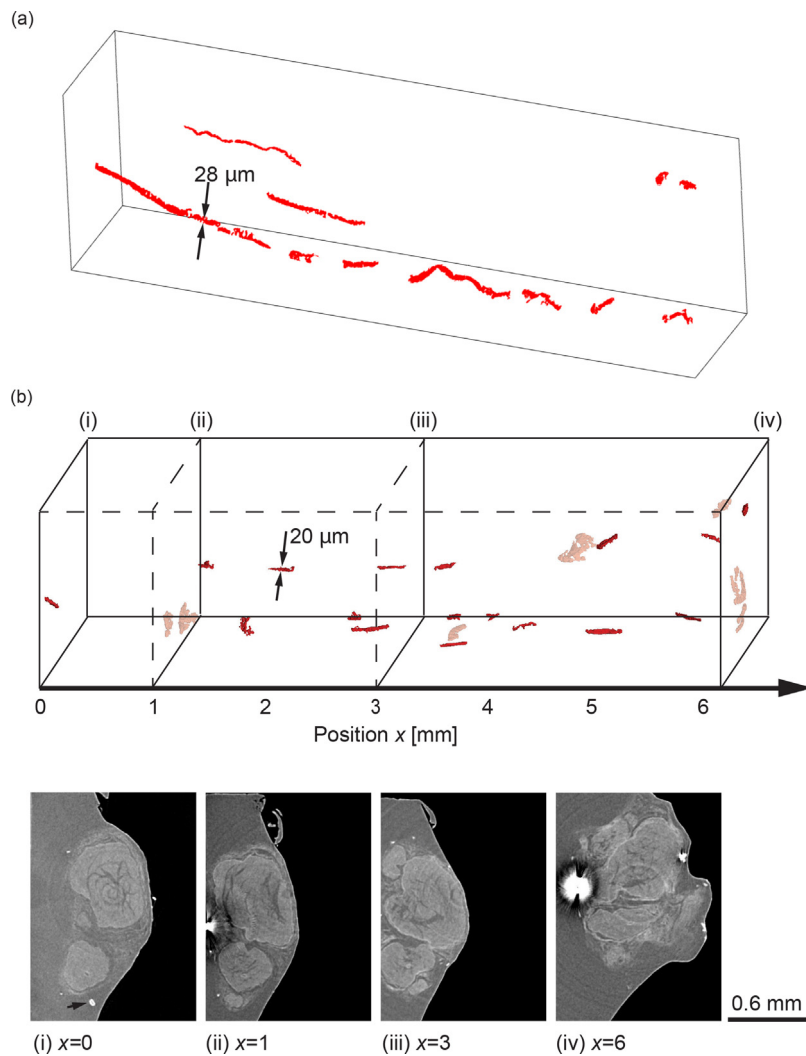

Fig. 5. The three-dimensional images (a) and (b) elucidate that the vessel tree is only partly revealed through a series of segments. The largest connected component in (a) has a volume of $1.9 \times 10^5 \, \mu m^3$ and an estimated mean diameter and length of 28 and 311 μm respectively. The four selected virtual sections (i–iv), assigned to the position within the three-dimensional representation of the segmented data (b), show that the vessel segments are characterized by high X-ray absorbing species given in white, as indicated for example by the arrow in (i). The streak artifacts, also appearing white in the virtual sections, can lead to false segmentation and were digitally made semi-transparent in the three-dimensional representation.

result of thermal irradiation from the X-ray source, the magnification was set to 25×, i.e., an effective pixel size of 4 μm. The spatial resolution was estimated close to 6 μm (Thurner et al., 2004). This result is an improvement of an order of magnitude with respect to

the study of Hopkins et al. (2015) in each of the three orthogonal directions.

It should be noted that paraffin embedding has advantages with respect to employing contrast-enhancing species such as Lugol's

iodine. The employment of highly X-ray-absorbing species necessitates higher accelerating voltages and generally impairs the image quality.

The contrast of the μCT data collected within the current study is surprisingly high, as soft-tissue components generally exhibit much less contrast than bony tissues. This is the result of local density and composition distributions. Here, the embedding of the nerve into paraffin, a mixture of hydrocarbons with a density of about $0.9\,g/cm^3$, is advantageous compared to the use of fixation fluid with a density of $1.0\,g/cm^3$. It is, however, important to avoid confined bubbles, which give rise to severe artifacts. Therefore, several trials to improve the paraffin embedding were tested, before a reasonable result could be found.

An important achievement of the present study is the nerve visualization inside the NC, which is a major challenge, since the NC material exhibits significantly higher X-ray absorption than the nerve tissue. The obtained μCT data, however, prove that both the microanatomy of the nerve inside the conduit and the porous structure of the scaffold are accessible in a reasonable manner.

Given that μCT is a non-destructive technique, conventional histology can be performed subsequently. In addition, contrarily to imaging approaches based on contrast agents, that require additional, time-consuming tissue processing steps, the presented approach requires hardly any adaptation of the standard histological paraffin-embedding protocol. Even in the best case scenario, where the iodine contrast agent can be removed without affecting histology, staining and de-staining the samples prior to and after imaging, respectively, needs at least four additional days of time. This time delay can be considerably increased, since incubation times are increasing with sample dimensions (Hopkins et al., 2015). Here, the μCT data can readily support the appropriate selection of the direction of the histological sections virtually cutting the tomography data (Stalder et al., 2014) and saving precious time. Anatomical landmarks guide the orientation and allow for the precise choice of the desired plane of interest.

A three-dimensional dataset with minimized artifacts is a prerequisite for the successful application of segmentation tools. Currently the segmentation is often carried out manually, which is time-consuming and error-prone due to the thousands of sections and the large size of data at the order of several gigabytes. Therefore, an increasing number of research teams employ computer software for segmentation and analysis tasks, see e.g., Long et al. (2014) and Irshad et al. (2014). The automatic procedure proposed in the present work is sufficiently accurate to extract geometrical characteristics of the nerve microanatomy even inside the higher X-ray absorbing conduit.

To underline the reliability of the segmentation, four selected sections were segmented manually and compared to the corresponding automatic result. The manual segmentation included the nervous and connective tissues and was based on visual inspection. Inclusions of the nervous tissue were considered in the manual segmentation only if thicker than 50 μm. The voxel segmentation resulted in 6% false positive and 17% false negative. The segmented area in the cross section shows an error of 11%. Thus, we assume an error of 11% in the volume measurement, as well.

The length of the computed centerline can be affected by the uncertainty of the cross section segmentation and the related error bars are given in Table 1. The minimal length was determined after smoothing with a moving average filter with a kernel size of 10 voxels and the maximal length was determined without smoothing.

It is well known, that a higher electron beam current within the source gives rise to a higher photon flux allowing for a shorter acquisition time due to increased photon statistics, see e.g. Holme et al. (2014). Therefore, one tries to work nearly the maximally possible beam current. Reducing the electron beam current, however,

one not only extends the lifetime of the filament, but also obtains higher spatial resolution because of the smaller cross-over (beam spot). The choice of the beam current is, therefore, an optimization task. For our study, we have found that 90% of the maximally possible beam current guarantees the necessary spatial resolution and photon statistics (contrast) at reasonable acquisition time. The acquisition time can be considerably shortened by means of a liquid jet anode (Bartels et al., 2013). Such an experimental setup also allows phase X-ray imaging, beneficial for the three-dimensional nerve visualization with increased contrast.

Nonetheless, the observed streak artifacts increase the error bars to about 15%, a value to be further optimized. Given that we have already optimized the selection of the appropriate scanning parameters, sample preparation itself needs to be further improved towards that goal. Avoiding high-absorbing species and cracks that can be present in the paraffin block, as well as trapped air bubbles, mainly on the nerve surface, will greatly reduce the presence of streak artifacts. Further efforts for refining our established procedure are under progress.

The vascular network is an essential component of healthy tissue, therefore the consideration of vessels in nerves is an important aspect of their evaluation. In this study, the feature-based filter for blood vessels was set up to detect tubular microstructures with a diameter starting from 8 μm, which corresponds to two voxel lengths. The application of the filter enabled us to detect blood vessels with a diameter larger than 12 μm. Nevertheless, the blood vessels of the formalin-fixated and paraffin-embedded tissue tend to collapse and are, therefore, less appropriate to estimate the spatial resolution reached within the present study. The vessel tree is only partly visible. Probably, only the remaining blood clots were made visible, which show relatively high X-ray absorption because of the iron present. These datasets already provide a reasonable estimate of the vessel density.

5. Conclusions

Advanced conventional μCT allows the three-dimensional characterization of paraffin-embedded nerves even inside a conduit of significantly higher X-ray absorption than the tissue. In spite of occurring streak artifacts, our approach employs fully automatic tools that yield reliable results. Consequently, reproducible non-destructive evaluations of specimen series have become possible in quantitative manner within hours (ref. publication 2). The method is fully compatible with established histology to be performed subsequent to the tomography measurements.

Conflicts of interest

The authors declare no conflict of interest.

Acknowledgements

References

Bartels, M., Hernandez, V.H., Krenkel, M., Moser, T., Salditt, T., 2013. Phase contrast tomography of the mouse cochlea at microfocus X-ray sources. Appl. Phys. Lett. 103, 083703, http://dx.doi.org/10.1063/1.4818737.

Bertelli, J.A., Taleb, M., Saadi, A., Mira, J.C., Pecot-Dechavassine, M., 1995. The rat brachial plexus and its terminal branches: an experimental model for the study of peripheral nerve regeneration. Microsurgery 16, 77–85.

Frangi, A.F., Niessen, W.J., Vincken, K.L., Viergever, M.A., 1998. Multiscale Vessel Enhancement Filtering. Springer Berlin Heidelberg, Berlin, Heidelberg, pp. 130–137, http://dx.doi.org/10.1007/BFb0056195.

Godinho, M.J., Teh, L., Pollett, M.A., Goodman, D., Hodgetts, S.I., Sweetman, I., Walters, M., Verhaagen, J., Plant, G.W., Harvey, A.R., 2013. Immunohistochemical, ultrastructural and functional analysis of axonal regeneration through peripheral nerve grafts containing Schwann cells expressing BDNF, CNTF or NT3. PLOS ONE 8, e69987, http://dx.doi.org/10.1371/journal.pone.0069987.

Hieber, S.E., Bikis, C., Khimchenko, A., Schweighauser, G., Hench, J., Chicherova, N., Schulz, G., Müller, B., 2016. Tomographic brain imaging with nucleolar detail and automatic cell counting. Sci. Rep. 6, 32156.

Holme, M.N., Schulz, G., Deyhle, H., Weitkamp, T., Beckmann, F., Lobrinus, J.A., Rikhtegar, F., Kurtcuoglu, V., Zanette, I., Saxer, T., Müller, B., 2014. Complementary X-ray tomography techniques for histology-validated 3D imaging of soft and hard tissues using plaque-containing blood vessels as examples. Nat. Protocols 9, 1401–1415, http://dx.doi.org/10.1038/nprot.2014.091.

Hopkins, T.M., Heilman, A.M., Liggett, J.A., LaSance, K., Little, K.J., Hom, D.B., Minteer, D.M., Marra, K.G., Pixley, S.K., 2015. Combining micro-computed tomography with histology to analyze biomedical implants for peripheral nerve repair. J. Neurosci. Methods 255, 122–130.

Irshad, H., Veillard, A., Roux, L., Racoceanu, D., 2014. Methods for nuclei detection, segmentation, and classification in digital histopathology: a review-current status and future potential. IEEE Rev. Biomed. Eng. 7, 97–114.

Kerschensteiner, M., Schwab, M.E., Lichtman, J.W., Misgeld, T., 2005. In vivo imaging of axonal degeneration and regeneration in the injured spinal cord. Nat. Med. 11, 572–577.

Khimchenko, A., Deyhle, H., Schulz, G., Schweighauser, G., Hench, J., Chicherova, N., Bikis, C., Hieber, S.E., Müller, B., 2016. Extending two-dimensional histology into the third dimension through conventional micro computed tomography. NeuroImage 139, 26–36.

Kroon, D.J., 2009. Hessian Based Frangi Vesselness Filter. http://www.mathworks.com/matlabcentral/fileexchange/24409-hessian-based-frangi-vesselness-filter.

Long, H.Q., Xie, W.H., Chen, W.L., Xie, W.L., Xu, J.H., Hu, Y., 2014. Value of micro-CT for monitoring spinal microvascular changes after chronic spinal cord compression. Int. J. Mol. Sci. 15, 12061–12073.

Madduri, S., Feldman, K., Tervoort, T., Papaloïzos, M., Gander, B., 2010a. Collagen nerve conduits releasing the neurotrophic factors GDNF and NGF. J. Controlled Release 143, 168–174, www.sciencedirect.com/science/article/pii/S0168365909008621.

Madduri, S., di Summa, P., Papaloïzos, M., Kalbermatten, D., Gander, B., 2010b. Effect of controlled co-delivery of synergistic neurotrophic factors on early nerve regeneration in rats. Biomaterials 31, 8402–8409, www.sciencedirect.com/science/article/pii/S0142961210008951.

Müller, B., Beckmann, F., Huser, M., Maspero, F., Székely, G., Ruffieux, K., Thurner, P., Wintermantel, E., 2002. Non-destructive three-dimensional evaluation of a polymer sponge by micro-tomography using synchrotron radiation. Biomol. Eng. 19, 73–78.

Müller, B., Deyhle, H., Lang, S., Schulz, G., Bormann, T., Fierz, F.C., Hieber, S.E., 2012. Three-dimensional registration of tomography data for quantification in biomaterials science. Int. J. Mater. Res. 103, 242–249, http://dx.doi.org/10.3139/146.110663.

Otsu, N., 1979. A threshold selection method from gray-level histograms. IEEE Trans. Syst. Man Cybern. 9, 62–66., http://dx.doi.org/10.1109/tsmc.1979.4310076.

Schneider, C.A., Rasband, W.S., Eliceiri, K.W., 2012. NIH Image to ImageJ: 25 years of image analysis. Nat. Methods 9, 671–675, http://dx.doi.org/10.1038/nmeth.2089.

Stalder, A.K., Ilgenstein, B., Chicherova, N., Deyhle, H., Beckmann, F., Müller, B., Hieber, S.E., 2014. Combined use of micro computed tomography and histology to evaluate the regenerative capacity of bone grafting materials. Int. J. Mater. Res. 105, 679–691, http://dx.doi.org/10.3139/146.111050.

Thurner, P., Beckmann, F., Müller, B., 2004. An optimization procedure for spatial and density resolution in hard X-ray micro-computed tomography. Nuclear Instrum. Methods Phys. Res. B 225, 599–603 http://www.sciencedirect.com/science/article/pii/S0168583X04007980.